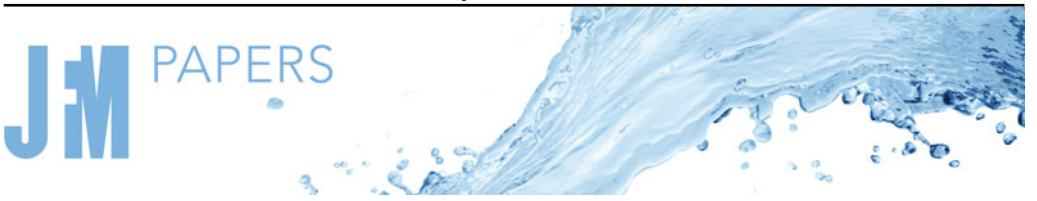
J. Fluid Mech. (2026), *vol.* 1037, A17, doi:10.1017/jfm.2026.11692



An attached-eddy elliptic approximation for two-dimensional structure functions in turbulent channel flow

Jiao Chen[1], **Xuebo Li**[1] **and Yongxiang Huang**[2]

[1]School of Mathematical Sciences, Chongqing University of Technology, Chongqing 400054, PR China

[2]Center for Marine Meteorology and Climate Change & College of Ocean and Earth Sciences, Xiamen University, Xiamen 361102, PR China

Corresponding author: Xuebo Li, xbl@cqut.edu.cn

(Received 1 January 2026 UTC; revised 14 April 2026 UTC; accepted 12 May 2026 UTC)

We investigate the equal-height, two-dimensional second-order structure function of the streamwise velocity fluctuation u in turbulent channel flow. Specifically, at a given wall-normal location z we consider $S_2(r_x, r_y; z) = \langle [u(x + r_x, y + r_y, z) - u(x, y, z)]^2 \rangle$, where (r_x, r_y) are the streamwise and spanwise separations in a wall-parallel plane and $\langle \cdot \rangle$ denotes wall-parallel spatial averaging. Focusing on separations within the logarithmic region, we build on Townsend's attached-eddy hypothesis and its hierarchical random additive-process formulation to introduce an attached-eddy elliptic approximation, in which the two-point geometry is represented by an elliptic in-plane footprint. The model yields a compact prediction for $S_2(r_x, r_y; z)$: its one-dimensional projections recover the canonical logarithmic forms with an asymptotically common slope, and its iso-S_2 contours at fixed z are predicted to be self-similar ellipses whose semi-axes scale linearly with z while maintaining an approximately constant aspect ratio (with mild finite-Reynolds-number effects). These predictions are assessed using direct numerical simulations at friction Reynolds numbers $Re_\tau = 1000$ and 5200, where $Re_\tau = u_\tau \delta / \nu$, and u_τ is the friction velocity, ν is the kinematic viscosity and δ is the channel half-height. When expressed in terms of r_i/z $(i = x, y)$, the projected structure functions collapse across wall-normal locations and vary linearly with $\ln(r_i/z)$. At fixed z, the iso-S_2 contours in the (r_x, r_y) plane are well described by ellipses characterised by a single anisotropy parameter $R = b/a$, where a and b are the ellipse semi-axes in the r_x and r_y directions, respectively. A simple level-dependent parameterisation of a and b provides an accurate and parsimonious reconstruction of the two-dimensional fields. Collectively, these results establish a geometrically transparent and quantitatively predictive framework

https://doi.org/10.1017/jfm.2026.11692 Published online by Cambridge University Press

© The Author(s), 2026. Published by Cambridge University Press.

for the two-dimensional organisation of wall-attached motions in the logarithmic region, extending attached-eddy concepts beyond traditional one-dimensional formulations.

Key words: turbulence theory, turbulent boundary layers, channel flow

1. Introduction

Statistical characterisations of the velocity field have long been central to turbulence research, and structure functions have remained a widely used tool for quantifying scale-dependent velocity increments. Following the seminal work of Kolmogorov (1941), scale invariance in the inertial subrange of three-dimensional, homogeneous and isotropic turbulence has been associated with scaling exponents that are commonly discussed under assumptions of local isotropy and local homogeneity (see, e.g. Karniadakis & Choi 2003; Marusic *et al.* 2010; Smits, McKeon & Marusic 2011, for reviews). In homogeneous and isotropic turbulence, second- and third-order structure functions, which quantify moments of velocity increments across a separation, have proved useful for diagnosing intermittency and anomalous scaling (Frisch & Kolmogorov 1995; Sreenivasan & Antonia 1997). In this setting, Kolmogorov's four-fifths law provides a rare exact result for locally isotropic turbulence in the inertial range, linking the third-order longitudinal structure function to the mean energy dissipation rate (Kolmogorov 1941; Lundgren 2002). In wall-bounded turbulence, however, strong mean shear and wall-normal inhomogeneity complicate a direct application of Kolmogorov's hypotheses and necessitate retaining inhomogeneous and anisotropic contributions in structure-function descriptions. This has motivated scale-dependent formulations that explicitly account for wall-normal position and directional anisotropy, and a substantial literature on structure functions in the presence of boundaries (Hill 2002; Casciola *et al.* 2003). Despite the added complexity of wall-bounded flows, structure functions continue to provide valuable insights into multiscale interactions, particularly when interpreted through attached-eddy models. Such models connect observed scaling behaviours to coherent, self-similar motions that populate the logarithmic (overlap) region (Davidson *et al.* 2006*b*; De Silva *et al.* 2015; Yang *et al.* 2017). The present study builds on this line of inquiry by revisiting the second-order structure-function formalism and extending it from a one-dimensional (1-D) to a two-dimensional (2-D) framework. Specifically, we develop an attached-eddy elliptic approximation (AEEA) that captures the in-plane statistical imprint of wall-attached motions, thereby revealing anisotropic scaling features and providing a parsimonious description of two-dimensional structure functions in the logarithmic region of high-Reynolds-number wall flows.

A defining feature of wall-bounded turbulence in the overlap (logarithmic) region, often referred to as the inertial sublayer, is the emergence of scale-invariant behaviour, most notably reflected in the logarithmic variation of the mean streamwise velocity with wall-normal distance. This feature has long underpinned predictive models of turbulent boundary layers (Smits *et al.* 2011; Jiménez 2012). The logarithmic region, typically located at intermediate wall-normal distances ($z^+ \gtrsim 100$), is populated by coherent motions whose statistical organisation has been successfully interpreted through the attached-eddy hypothesis (AEH) originally proposed by Townsend (1976). According to the AEH, the turbulent velocity field may be viewed as a superposition of wall-attached eddies whose characteristic sizes scale linearly with distance from the wall, thereby yielding self-similar scaling in both physical and spectral space. Empirical and numerical studies have provided substantial support for this picture. In particular, the streamwise variance exhibits an approximately logarithmic dependence on wall-normal position, commonly expressed as $\langle u^2 \rangle \sim A_1 \ln(\delta/z) + B_1$, where A_1 is the Townsend–Perry logarithmic coefficient for

https://doi.org/10.1017/jfm.2026.11692 Published online by Cambridge University Press

the streamwise variance, δ is the channel half-height, and B_1 is the additive constant (intercept) in the logarithmic variance law, consistent with hierarchies of self-similar wall-attached motions (Hultmark 2012; Marusic *et al.* 2013; De Silva *et al.* 2015; Marusic & Monty 2019; Baars & Marusic 2020). The model was further refined by Perry & Chong (1982), who introduced explicit eddy forms to enable quantitative predictions of turbulence statistics. Moreover, the persistence of logarithmic $\langle u^2 \rangle$ scaling across a finite range of z provides additional evidence for scale-separated wall-attached motions in the logarithmic region (Perry, Henbest & Chong 1986; Marusic *et al.* 2013; Baars & Marusic 2020).

The AEH for energy-containing motions in wall-bounded flows is analogous, in spirit, to hierarchical cascade models for homogeneous isotropic turbulence (Frisch & Kolmogorov 1995; Jiménez 2012). It provides a statistical description of the large-scale motions by prescribing a population of randomly distributed, wall-attached, momentum-transferring eddies within a specified range of sizes. These eddies are assumed to share a characteristic shape, with a number density that depends on the distance from the wall. Within this construction, the AEH yields scaling predictions for a range of turbulence statistics in wall-bounded flows, and it also provides a natural basis for interpreting structure functions in flows that depart from strict homogeneity and isotropy. Complementary theoretical developments, such as those of Hill (2002) and Cimarelli *et al.* (2016), extend Kolmogorov-type relations to wall-bounded turbulence by retaining inhomogeneous contributions in the budgets of second- and higher-order structure functions. In this context, we consider the equal-height, two-dimensional second-order structure function of the streamwise velocity fluctuation

$$S_2(r_x, r_y; z) = \left\langle \left[u(x + r_x, y + r_y, z) - u(x, y, z) \right]^2 \right\rangle, \tag{1.1}$$

where u denotes the streamwise velocity fluctuation, (r_x, r_y) are the streamwise and spanwise separations, respectively, and $\langle \cdot \rangle$ denotes an ensemble average (implemented here as averaging over (x, y, t) at fixed z). The function S_2 therefore encodes both the directional anisotropy and the scale dependence of streamwise fluctuations at a given wall-normal location.

Experimental evidence for structure-function scaling in the logarithmic region has been reported by Davidson *et al.* (2006*a*, *b*), Davidson & Krogstad (2009, 2014), who observed an approximately logarithmic dependence of S_2 on r_x for separations in the energy-containing range, with $r_x = O(z)$. More recently, De Silva *et al.* (2015) extended this analysis to higher-order moments and used AEH-based arguments to rationalise the observed behaviours. A further advance was made by Yang *et al.* (2016, 2017), who developed a stochastic additive-process model grounded in the AEH to describe structure-function scaling across velocity components and two-point directions. Their model, which encodes the statistical imprint of hierarchies of self-similar wall-attached motions, successfully predicts the observed 1-D structure-function behaviour. However, the corresponding 2-D structure function in the (r_x, r_y) plane has received comparatively little attention, particularly in terms of an explicit geometric representation based on the AEH. To address this gap, the present study builds on the 1-D structure-function scaling description within the AEH/hierarchical random additive-process (HRAP) picture and develops an AEEA for the equal-height, wall-parallel 2-D structure function. Specifically, we introduce an elliptic approximation to describe the in-plane footprint of wall-attached motions (and its relation to their geometric inclination), thereby providing a more complete characterisation of the wall-parallel anisotropic organisation of the 2-D structure function in the logarithmic region. These developments are assessed using direct numerical simulation (DNS) data at high Reynolds numbers.

https://doi.org/10.1017/jfm.2026.11692 Published online by Cambridge University Press

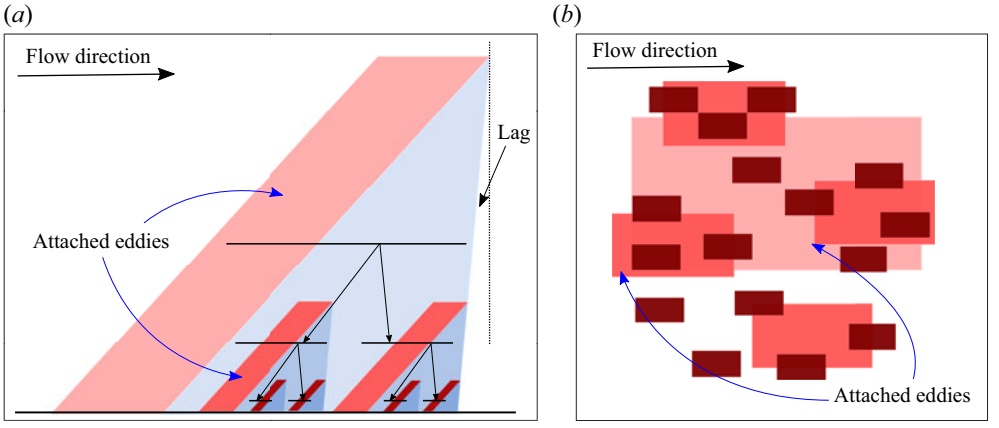


Figure 1. Conceptual schematic of the attached-eddy picture for wall-bounded turbulence. (*a*) Inclined wall-attached eddies, represented as parallelograms (schematic, not to scale) in the (x, z) plane, where x and z denote the streamwise and wall-normal directions. Three hierarchical levels are indicated by increasing shades of red; the blue shaded regions illustrate their cumulative influence at a given height. The inclination reflects the observed tilt of coherent motions between two wall-normal locations. (*b*) Plan view of the logarithmic region in the (x, y) plane, where y is the spanwise direction. A random superposition of eddies of different sizes illustrates the hierarchical organisation; colours denote different wall-normal extents.

Figure 1 summarises the self-similar hierarchy of wall-attached eddies envisioned by the AEH (Townsend 1976). Figure 1(*a*) depicts inclined eddies in the (x, z) plane, consistent with the observed tilt of coherent motions in wall turbulence (Adrian 2007), whereas figure 1(*b*) shows a plan view of the logarithmic region populated by streamwise-elongated structures spanning a range of sizes. The colour coding indicates the hierarchical organisation: larger structures extend farther from the wall and exhibit proportionally larger streamwise and spanwise footprints, consistent with approximately self-similar scaling across the logarithmic region (Baars, Hutchins & Marusic 2017). Building on this framework, Yang *et al.* (2017) proposed a stochastic HRAP model that yields quantitative predictions for the scaling of the second-order structure-function tensor across velocity components and separation directions. Their formulation recovers the classical z-scaling for streamwise separations and provides additional constraints on spanwise and wall-normal dependencies, thereby extending the structure-function framework to a multidirectional setting. However, their analysis was largely restricted to 1-D representations of $D_{ij}(r; z)$. The present study extends these ideas to a 2-D formulation that explicitly captures the anisotropic scaling footprint of wall-attached motions in the (r_x, r_y) plane.

This extension is motivated by the spatial organisation of wall turbulence: coherent motions exhibit elongated streamwise footprints and a characteristic inclination relative to the wall, which can manifest as an approximately elliptical organisation of two-point statistics in wall-parallel planes (Del Alamo *et al.* 2004; Chandran *et al.* 2017). Related studies suggest that, in second-order statistical descriptions of turbulent shear flows, both space–time correlations and the contour organisation implied by space–time spectral models can naturally exhibit an approximately elliptic geometry (Favre, Gaviglio & Dumas 1958; He & Zhang 2006; Wilczek, Stevens & Meneveau 2015; He, Jin & Yang 2017). Motivated by this viewpoint, we adopt the idea that an ellipse may serve as an effective geometric approximation for two-point statistical contours, and reformulate it here as the wall-parallel level-set geometry of the equal-height 2-D structure function within the AEH/HRAP framework. We therefore introduce a phenomenological elliptic

https://doi.org/10.1017/jfm.2026.11692 Published online by Cambridge University Press

approximation as the defining geometric ingredient of AEEA in which iso-contours of the equal-height, 2-D streamwise structure function $S_2(r_x, r_y; z)$ are modelled as self-similar ellipses over the logarithmic region. Here, the ellipse should be interpreted as an effective statistical geometry of the iso-S_2 sets in the (r_x, r_y) plane, rather than as the exact boundary of an individual instantaneous attached structure. This construction builds directly on the 1-D HRAP framework and provides a natural geometric generalisation consistent with both physical observations and theoretical expectations. To assess its validity, we analyse DNS datasets of turbulent channel flow at friction Reynolds numbers $Re_\tau = 1000$ and 5200 (Lee & Moser 2015; Graham *et al.* 2016) (with $Re_\tau = u_\tau \delta/\nu$). Here, (x, y, z) denote the streamwise, spanwise and wall-normal directions, respectively, and u is the streamwise velocity fluctuation. While the present analysis is necessarily constrained by the Reynolds numbers available in the DNS datasets used to evaluate S_2, future simulations at higher Re_τ will permit a more stringent assessment of the proposed scaling relations and their range of applicability. In particular, the influence of very-large-scale motions and any departures from strict geometric self-similarity at ultra-high Reynolds numbers remain open questions.

2. Datasets

We analyse two canonical DNS of incompressible turbulent channel flow at friction Reynolds numbers $Re_\tau = 1000$ and 5200, obtained from the Johns Hopkins Turbulence Database (Lee & Moser 2015; Graham *et al.* 2016). Here, $Re_\tau \equiv u_\tau \delta/\nu$, where u_τ is the friction velocity, ν the kinematic viscosity and δ the channel half-height. Both simulations employ a pseudo-spectral discretisation with periodic boundary conditions in the streamwise and spanwise directions and no-slip walls at $z = 0$ and $z = 2\delta$. The computational domain is $L_x \times L_y \times L_z = 8\pi\delta \times 3\pi\delta \times 2\delta$. Details of numerical resolution, dealiasing and validation are reported by Lee & Moser (2015), and these databases have been widely used and assessed in prior work (Marusic *et al.* 2013; Baars & Marusic 2020; Li, Wang & Zheng 2021).

In addition to the channel flow DNS, we also incorporate a set of atmospheric surface layer (ASL) measurements for supplementary comparison. The dataset was collected during the SLTEST field campaign over the salt flats in western Utah, USA, from 26 May to 4 June 2005, and its measurement characteristics and processing procedures have been documented in detail (Marusic & Heuer 2007; Marusic & Hutchins 2008; Hutchins *et al.* 2012; Chauhan *et al.* 2013). The experiment employed nine Campbell Scientific CSAT3 sonic anemometers mounted on a vertical mast with logarithmically spaced heights spanning $z_R = 1.41$ to $z_T = 25.69$ m, corresponding to an atmospheric boundary-layer thickness of approximately $\delta \approx 60$ m (corresponding to $Re_\tau \approx 6 \times 10^5$). The three velocity components (u, v, w) and temperature were sampled at 20 Hz. In addition, a cross-stream array of sonic anemometers was deployed at $z = 2.14$ m over a 30 m span to improve statistical convergence. It is important to emphasise that the main analyses and model fitting throughout the paper are based on the DNS; the ASL data are used only in the final Reynolds-number comparison. To minimise buoyancy effects, we identify near-neutral periods using the Monin–Obukhov stability parameter z/L (Obukhov 1946; Monin & Obukhov 1954) and select intervals satisfying $|z/L| < 0.01$, yielding 10 one-hour samples. For these ASL samples, the streamwise separation r_x is not obtained from direct spatial measurements, but is converted from the temporal delay using Taylor's frozen-turbulence hypothesis, namely $r_x = U_c \tau$, where τ is the time delay and U_c is taken as the one-hour mean streamwise velocity at the corresponding measurement height. On this basis, we extract the logarithmic slope coefficient P_x of the streamwise structure

https://doi.org/10.1017/jfm.2026.11692 Published online by Cambridge University Press

function (with $P_x = 2A_1$ in (3.9)) and compare it with the DNS-based estimates to assess Reynolds-number dependence.

Wall-parallel planes are extracted at wall-normal locations within the logarithmic region, $\nu/u_\tau \ll z \ll \delta$. At each z, we form the streamwise velocity fluctuation $u(x, y, z, t) = U(x, y, z, t) - \langle U \rangle_{x,y,t}(z)$, and pre-normalise by u_τ so that the resulting structure function is dimensionless. Assuming in-plane homogeneity, ensemble averages are implemented as averages over (x, y, t) at fixed z. The equal-height, two-dimensional second-order structure function $S_2(r_x, r_y; z)$ is evaluated for wall-parallel separations $\boldsymbol{r} = (r_x, r_y, 0)$ and is defined as in (1.1). In practice, S_2 is computed on the full in-plane grid using the spectral method described in Appendix A, which exploits periodicity and preserves energy consistency. To avoid wrap-around artefacts associated with the finite periodic domain, reported separations satisfy $|r_x| \leqslant L_x/2$ and $|r_y| \leqslant L_y/2$.

For comparison with attached-eddy predictions, we consider a set of representative wall distances in inner units $z^+ \equiv z u_\tau/\nu$. Specifically, for $Re_\tau = 1000$ we use $z^+ = \{80, 100, 110, 140, 150\}$, and for $Re_\tau = 5200$ we use $z^+ = \{250, 300, 400, 500, 600\}$ (as in figures 2–4). These locations lie within the overlap region, sufficiently separated from both the viscous sublayer and the outer-layer influence (Marusic *et al.* 2013). Unless stated otherwise, lengths are reported in outer units (scaled by δ), while velocities are scaled by u_τ.

3. Two-dimensional second-order structure function: an attached-eddy elliptic approximation

Building on Townsend's AEH and its HRAP realisation (Townsend 1976; Yang *et al.* 2017), we develop a closed prediction for the equal-height, wall-parallel second-order structure function of the streamwise velocity fluctuation in the logarithmic region within the AEEA framework. We employ Cartesian coordinates (x, y, z) for the streamwise, spanwise and wall-normal directions, and denote wall-parallel position by $\boldsymbol{x} = (x, y)$ and wall-parallel separation by $\boldsymbol{r} = (r_x, r_y, 0)$. Throughout, we restrict attention to equal-height statistics ($r_z = 0$) with both points at a wall distance z satisfying $\nu/u_\tau \ll z \ll \delta$. The fluctuation $u(\mathbf{x}, z)$ is defined as the deviation from the mean streamwise velocity at the same z, and $\langle \cdot \rangle$ denotes averaging at fixed z, implemented here as in-plane spatial averaging over (x, y). The equal-height 2-D structure function is defined in (1.1) and is not repeated here.

Within the AEH/HRAP framework, $S_2(\boldsymbol{r}; z)$ admits a transparent interpretation: it accumulates the contributions of wall-attached motions that are not simultaneously sampled at the two points, while motions whose footprints cover both points cancel in the increment. The only additional ingredient needed to close the prediction is the wall-parallel geometry that determines the minimal eddy height required to cover both points for a given separation $\boldsymbol{r}$.

3.1. *The AEH/HRAP foundation: cumulative contributions and the one-dimensional law*

In the attached-eddy picture, wall-attached motions form a self-similar hierarchy parameterised by their height z' (measured from the wall to the eddy top), which sets all other relevant length scales. The number density of eddies with heights in $(z', z' + \mathrm{d}z')$ per unit wall-parallel area is modelled as

$$\rho(z')\,\mathrm{d}z' = \frac{C_\rho}{z'}\,\mathrm{d}z', \qquad \nu/u_\tau \ll z' \ll \delta, \tag{3.1}$$

https://doi.org/10.1017/jfm.2026.11692 Published online by Cambridge University Press

where the $1/z'$ dependence expresses scale invariance on logarithmic bands of z' in the hierarchy (Perry & Chong 1982; Perry *et al.* 1986). Let $\chi(\boldsymbol{x}; z', z) \in \{0, 1\}$ indicate whether the point $(\boldsymbol{x}, z)$ lies within the wall-parallel footprint of an attached eddy of height z'. The streamwise fluctuation at height z may then be represented schematically as a superposition over eddy heights

$$u(\boldsymbol{x}, z) = \int_z^\delta a(z')\, \chi(\boldsymbol{x}; z', z)\, \rho(z')\, \mathrm{d}z', \tag{3.2}$$

where $a(z')$ is a zero-mean random amplitude. Following Yang *et al.* (2017), we assume: (i) $\langle a(z')\rangle = 0$; (ii) the variance is approximately constant when binned on logarithmic bands, i.e. $\langle a^2(z')\rangle \simeq \sigma^2$ within each band; and (iii) inter-band correlations are weak at leading order and are neglected in the present scaling arguments.

Counting the active logarithmic bands yields the Townsend–Perry logarithmic variance law (Marusic *et al.* 2013; Marusic & Monty 2019; Baars & Marusic 2020)

$$\langle u^2(z)\rangle = \sigma^2 \int_z^\delta \rho(z')\, \mathrm{d}z' + B_1 = A_1\, \ln\left(\frac{\delta}{z}\right) + B_1, \qquad A_1 = \sigma^2 C_\rho, \tag{3.3}$$

where B_1 accounts for finite-Re_τ corrections.

For two points at the same height z separated by $\boldsymbol{r}$, an eddy of height z' contributes to the increment $u(\boldsymbol{x}+\boldsymbol{r}, z) - u(\boldsymbol{x}, z)$ only if it covers exactly one of the two points. Let $\tilde{z}_c(\boldsymbol{r})$ denote the geometric shared-eddy height: the minimal eddy height whose wall-parallel footprint can simultaneously cover both points at separation $\boldsymbol{r}$. Eddies with $z \leqslant z' < \tilde{z}_c$ are unshared and contribute additively to the increment variance, whereas those with $z' \geqslant \tilde{z}_c$ are shared and cancel in the increment. Accounting for the inner cutoff at z and the outer cutoff at δ yields the compact HRAP form

$$\begin{aligned} S_2(\boldsymbol{r}; z) &= 2\,\sigma^2 \int_z^{z_e(\boldsymbol{r})} \rho(z')\, \mathrm{d}z' + C_{11} = 2A_1\, \ln\left(\frac{z_e(\boldsymbol{r})}{z}\right) + C_{11}, \\ z_e(\boldsymbol{r}) &= \max\Big\{ z,\ \min\big[\, \tilde{z}_c(\boldsymbol{r}),\ \delta \,\big] \Big\}. \end{aligned} \tag{3.4}$$

Here, C_{11} is an additive offset representing finite-Re_τ and small-scale contributions not described by the energy-containing attached-eddy approximation. In particular, the apparent 'small-separation plateau' $S_2 \simeq C_{11}$ is a consequence of the present energy-containing model and should not be interpreted as the viscous limit $|\boldsymbol{r}| \to 0$. If one wishes to enforce the large-separation constraint $S_2(\boldsymbol{r}; z) \to 2\langle u^2(z)\rangle$ as $|\boldsymbol{r}| \to \infty$, then (3.4) implies the calibration $C_{11} = 2B_1$; otherwise, (3.4) remains a consistent logarithmic model within its validity range.

3.2. *Geometry of shared eddies: from one to two dimensions*

To close (3.4), we specify $\tilde{z}_c(\boldsymbol{r})$ from the wall-parallel geometry implied by attached motions. Let $\theta \in (0, \pi/2)$ denote the mean inclination of an attached eddy to the wall, such that a representative streamwise footprint scale grows as $z'/\tan\theta$. Planform anisotropy is introduced through a spanwise-to-streamwise footprint ratio $R > 0$ (with $R > 1$ corresponding to wider spanwise footprints at fixed streamwise extent). The 1-D limits along the principal directions require

$$\tilde{z}_c(r_x, 0) = |r_x|\, \tan\theta, \qquad \tilde{z}_c(0, r_y) = \frac{|r_y|\, \tan\theta}{R}, \tag{3.5}$$

https://doi.org/10.1017/jfm.2026.11692 Published online by Cambridge University Press

which define the streamwise and spanwise cross-over lengths $\ell_x = z/\tan\theta$ and $\ell_y = Rz/\tan\theta$, respectively.

A simple closure consistent with (3.5) is the max-norm footprint (Yang *et al.* 2017)

$$\tilde{z}_c^{(\infty)}(r_x, r_y) = \tan\theta \ \max\left(|r_x|, \frac{|r_y|}{R}\right), \tag{3.6}$$

whose iso-$\tilde{z}_c$ contours are diamonds in the (r_x, r_y) plane. Although this choice preserves the 1-D limits along the principal directions, it is non-differentiable along the axes and does not directly provide a continuous in-plane representation suitable for the equal-height 2-D structure-function level sets, which here correspond fundamentally to loci of fixed shared-eddy critical height in the (r_x, r_y) plane. We therefore adopt a smooth elliptic (Euclidean) metric that preserves (3.5) and closes the wall-parallel shared-eddy mapping

$$\tilde{z}_c^{(2)}(r_x, r_y) = \tan\theta \sqrt{r_x^2 + \left(\frac{r_y}{R}\right)^2}. \tag{3.7}$$

The purpose of this choice is not only to regularise the off-axis geometry, but also, while retaining the principal-direction limits, to make the level sets of $S_2(r_x, r_y; z)$ explicitly representable as a family of analytic geometric objects. In this way, the 2-D geometry enters the model in a unified manner through the mapping $\boldsymbol{r} \mapsto \tilde{z}_c(\boldsymbol{r})$; the outer cutoff at δ is still imposed only once, via $z_e(\boldsymbol{r})$ in (3.4).

Substituting (3.7) into (3.4), and restricting to separations for which $z < \tilde{z}_c^{(2)}(r_x, r_y) < \delta$ (so that $z_e = \tilde{z}_c^{(2)}$), yields the AEEA

$$S_2^{(ell)}(r_x, r_y; z) = 2A_1 \ \ln\left[\frac{\tan\theta}{z}\sqrt{r_x^2 + \left(\frac{r_y}{R}\right)^2}\right] + C_{11}. \tag{3.8}$$

As $\tilde{z}_c^{(2)} \to \delta$ (equivalently, as $z_e \to \delta$), (3.4) implies saturation to the large-separation plateau $2A_1 \ln(\delta/z) + C_{11}$.

3.3. *Rigorous reduction: two dimensions → one dimension and piecewise domains*

The 2-D closure recovers the canonical 1-D HRAP laws along the principal directions and delineates the piecewise domains induced by the outer cutoff at δ.

Along the streamwise axis ($r_y = 0$), (3.7) gives $\tilde{z}_c^{(2)} = \tan\theta\,|r_x|$, and hence $z_e = \max\{z, \min[\tan\theta|r_x|, \delta]\}$. Introducing the cross-over length $\ell_x = z/\tan\theta$ yields

$$S_2(r_x, 0; z) = \begin{cases} C_{11}, & |r_x| < \ell_x, \\ 2A_1 \ \ln\big(|r_x|/\ell_x\big) + C_{11}, & \ell_x \leqslant |r_x| \leqslant \delta/\tan\theta, \\ 2A_1 \ \ln\big(\delta/z\big) + C_{11}, & |r_x| > \delta/\tan\theta. \end{cases} \tag{3.9}$$

The small-separation branch $S_2 \simeq C_{11}$ is the energy-containing attached-eddy approximation and should not be interpreted as the viscous $r \to 0$ limit.

Likewise, along the spanwise axis ($r_x = 0$), (3.7) gives $\tilde{z}_c^{(2)} = \tan\theta\,|r_y|/R$, and the cross-over length is $\ell_y = Rz/\tan\theta = R\,\ell_x$. Therefore,

$$S_2(0, r_y; z) = \begin{cases} C_{11}, & |r_y| < \ell_y, \\ 2A_1 \ \ln\big(|r_y|/\ell_y\big) + C_{11}, & \ell_y \leqslant |r_y| \leqslant R\delta/\tan\theta, \\ 2A_1 \ \ln\big(\delta/z\big) + C_{11}, & |r_y| > R\delta/\tan\theta. \end{cases} \tag{3.10}$$

https://doi.org/10.1017/jfm.2026.11692 Published online by Cambridge University Press

Thus, both 1-D projections share the same logarithmic slope $2A_1$, where A_1 denotes the classical Townsend–Perry constant, taken here as $A_1 \approx 1.25$, while the cross-over scales are set by (θ, R). The choice of in-plane metric affects only the off-axis geometry; the principal-direction limits in (3.9)–(3.10) remain unchanged.

3.4. *Iso-levels and geometric self-similarity in the wall-parallel plane*

Beyond the 1-D projections, the elliptic closure provides an explicit description of equal-height two-point geometry in the (r_x, r_y) plane. For fixed z and separations in the intermediate range $z < \tilde{z}_c^{(2)}(r_x, r_y) < \delta$, the iso-levels $S_2^{(ell)}(r_x, r_y; z) = D^\star$ follow by inverting (3.8), yielding a family of self-similar ellipses

$$\frac{r_x^2}{a^2} + \frac{r_y^2}{b^2} = 1, \qquad a(z; D^\star) = \frac{z}{\tan\theta}\,\exp\!\Big(\tfrac{D^\star - C_{11}}{2A_1}\Big), \qquad b(z; D^\star) = R\,a(z; D^\star), \tag{3.11}$$

where a and b are the semi-axes in the r_x and r_y directions, respectively. Here, $\ell_x = z/\tan\theta$ and $\ell_y = Rz/\tan\theta$ denote the cross-over scales along the principal directions, whereas a and b denote the semi-axes of the corresponding elliptic iso-contour at a prescribed level $D^\star$. Thus, a and b may be understood as the elliptic semi-axes determined from these baseline scales through the same level-dependent factor. The admissible levels are bounded by the intermediate-range logarithmic branch and the large-separation cap

$$C_{11} \leqslant D^\star \leqslant 2A_1 \ln(\delta/z) + C_{11}. \tag{3.12}$$

The lower bound corresponds to the energy-containing plateau of the model and should not be interpreted as the viscous $|\boldsymbol{r}| \to 0$ limit.

Equation (3.11) implies that, for any fixed level $D^\star$, the ellipse semi-axes scale linearly with z, while the aspect ratio $b/a = R$ is independent of z. Equivalently,

$$\frac{a}{z} = \frac{1}{\tan\theta}\,\exp\!\Big(\tfrac{D^\star - C_{11}}{2A_1}\Big), \qquad \frac{b}{z} = \frac{R}{\tan\theta}\,\exp\!\Big(\tfrac{D^\star - C_{11}}{2A_1}\Big), \tag{3.13}$$

so that the iso-levels are geometrically self-similar throughout the logarithmic region: the enclosed area scales as $ab \propto z^2$, while the eccentricity is determined solely by R. This indicates that, at fixed level, the 2-D iso-contours may be understood as a family of in-plane contours controlled by the shared-eddy cutoff and expanding with the same height scale along the two principal directions. In the isotropic limit $R \to 1$, the iso-levels reduce to concentric circles.

For comparison, the max-norm closure (3.6) produces diamond-shaped iso-levels in the (r_x, r_y) plane. Importantly, the intercepts on the coordinate axes coincide with those implied by (3.11), so both closures share the same 1-D limits and the same level-set scales; the elliptic metric simply regularises the off-axis geometry.

3.5. *Scope and parameter roles*

The elliptic closure (3.8) applies to equal-height, wall-parallel separations ($r_z = 0$) with both points in the logarithmic region and with separations in the intermediate range $z < \tilde{z}_c^{(2)}(r_x, r_y) < \delta$ (equivalently, $z < z_e(\boldsymbol{r}) < \delta$). As $z_e \to \delta$, (3.4) implies saturation to the large-separation plateau $2A_1 \ln(\delta/z) + C_{11}$. For sufficiently small separations, the energy-containing attached-eddy approximation ceases to apply and inertial or viscous behaviour supersedes the logarithmic form; if desired, one may append a standard composite correction (e.g. an inertial $|\boldsymbol{r}|^{2/3}$ or viscous $|\boldsymbol{r}|^2$ segment) without modifying the present finite-separation closure.

https://doi.org/10.1017/jfm.2026.11692 Published online by Cambridge University Press

The four parameters (A_1, C_{11}, θ, R) play distinct and complementary roles. The parameter A_1 sets the common logarithmic slope in the 1-D reductions (3.9)–(3.10), consistent with the variance law (3.3). The inclination θ determines the streamwise cross-over $\ell_x = z/\tan\theta$ (and hence the mapping from in-plane separations to the shared-eddy height); R simultaneously controls the spanwise cross-over scale, $\ell_y = R\ell_x$, and the in-plane shape anisotropy, namely the aspect ratio $b/a = R$. A larger R corresponds to contours that are relatively broader in the spanwise direction, whereas a smaller R corresponds to ellipses that are relatively more elongated in the streamwise direction. Finally, C_{11} fixes the vertical offset of S_2 and the correspondence between a prescribed level $D^\star$ and the ellipse size in (3.11); choosing $C_{11} = 2B_1$ aligns the large-separation plateau with $2\langle u^2(z)\rangle$.

In summary, the HRAP construction reduces the equal-height structure function to the counting of non-shared attached eddies between z and $z_e(\boldsymbol{r})$, while the elliptic planform (3.7) provides a smooth 2-D closure. The resulting model recovers the established 1-D limits, predicts self-similar iso-levels in the wall-parallel plane, and furnishes a compact framework for analysing the anisotropic organisation of wall-attached motions in the logarithmic region.

4. Results

4.1. *Height similarity of one-dimensional structure functions*

A central prediction of the elliptic closure derived in § 3 (AEEA) is that the 1-D projections of the equal-height structure function exhibit height similarity in the logarithmic region when expressed in terms of the normalised separation r_i/z $(i = x, y)$. In particular, the logarithmic branches of the piecewise relations (3.9)–(3.10) imply that, over the intermediate range between the cross-over and the outer cutoff, S_2 varies linearly with $\ln(r_i/z)$ with a common slope set by $2A_1$, while the cross-over locations scale with z (see § 3.2). We assess these predictions using the two channel-flow databases described in § 2. Throughout this section, the fluctuation field is normalised by u_τ, so that S_2 is dimensionless.

Figure 2 shows the projected structure functions plotted against r_x/z and r_y/z for several z^+ in the logarithmic region at both Reynolds numbers. In each panel, the curves at different z^+ collapse closely when expressed in terms of r_i/z, supporting the predicted height similarity and the linear z-scaling of the cross-over lengths implicit in (3.9)–(3.10). Over the fitted interval $2 \leqslant S_2 \leqslant 4$, the projections vary approximately linearly with $\ln(r_i/z)$, consistent with the logarithmic branches of (3.9) and (3.10). The interval $2 \leqslant S_2 \leqslant 4$ is adopted here as the fitting window in order to focus as much as possible on the intermediate logarithmic-growth range, while avoiding, as far as possible, the significant influence of the cross-over at small separations and the approach to the outer cap at large separations, thereby maintaining a consistent fitting basis across different wall-normal locations and different directions.

The fitted slopes annotated in figure 2 quantify the effective logarithmic growth within the available overlap range. For $Re_\tau = 1000$, the fits yield $P = 1.71$ for the streamwise projection and $P = 2.87$ for the spanwise projection; for $Re_\tau = 5200$ the corresponding values are $P = 1.56$ and $P = 2.41$. Thus, while both directions exhibit clear height similarity, the fitted slopes depend on direction and decrease mildly with Reynolds number over the present fitting window. These differences are consistent with finite-Reynolds-number limitations: within the presently available scale-separation range, even with the intermediate window adopted above, the fitted results remain unavoidably influenced by the transition regions on either side of the logarithmic branch. These transitions occur at

https://doi.org/10.1017/jfm.2026.11692 Published online by Cambridge University Press

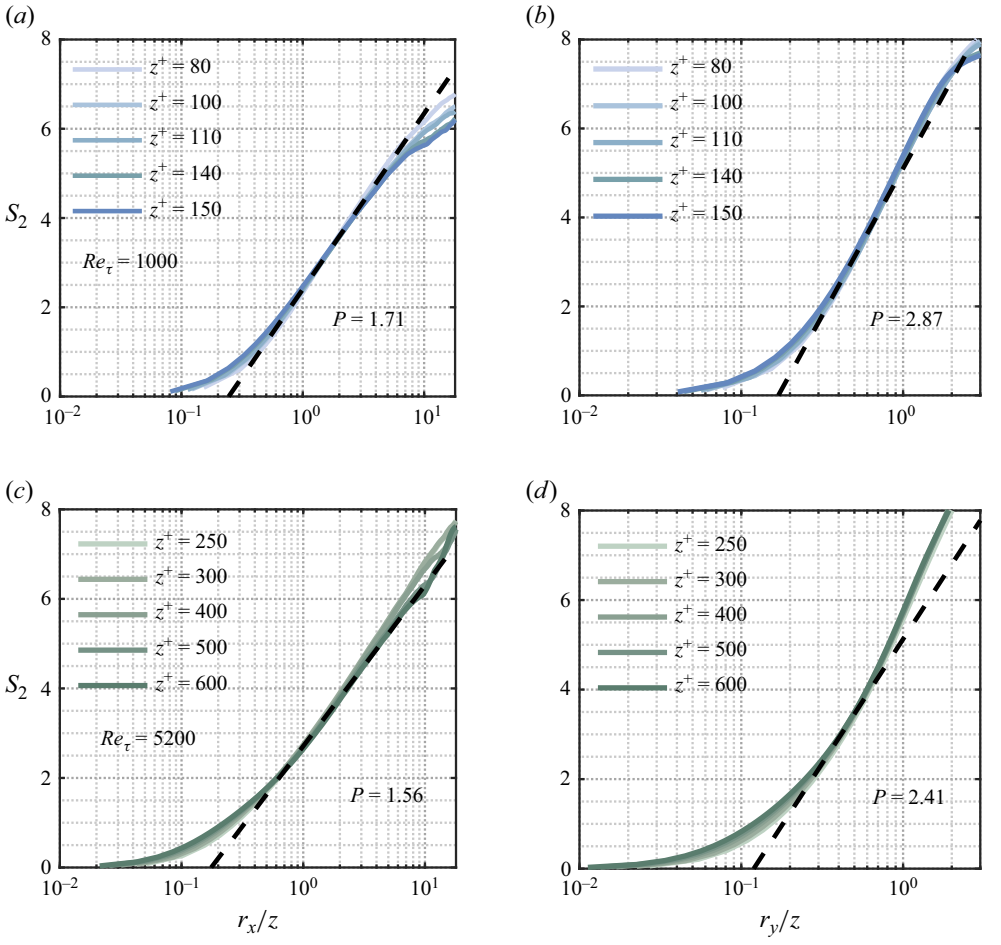


Figure 2. One-dimensional projections of the equal-height second-order structure function in the logarithmic region: (*a*, *b*) $Re_\tau = 1000$; (*c*, *d*) $Re_\tau = 5200$. (*a*,*c*) $S_2(r_x, 0; z)$ versus r_x/z; (*b*,*d*) $S_2(0, r_y; z)$ versus r_y/z. Colours denote different wall-normal locations z^+ within the logarithmic layer (see § 2). Black dashed lines show least-squares fits of S_2 against $\ln(r_i/z)$ over the interval $2 \leqslant S_2 \leqslant 4$; the fitted slope P (to be compared with the asymptotic prediction $P = 2A_1 = 2.5$) is indicated in each panel.

different r_i/z locations in the two directions because both the cross-over and the outer limit are anisotropic (cf. § 3.2). A more systematic parameter extraction and the associated 2-D consistency checks are presented in the following subsections.

Figure 3 complements figure 2 by visualising the projected structure functions as contour maps in the $(r_i/\delta,\ z/\delta)$ plane. In the logarithmic branches of (3.9)–(3.10), a fixed contour level implies a fixed value of $r_i/\ell_i(z)$; since the cross-over lengths scale linearly with z (cf. § 3.2), the corresponding iso-levels are therefore predicted to align with $r_i/z =$ const, i.e. straight lines of unit slope on log–log axes. The contours in figure 3 exhibit this organisation over a substantial portion of the overlap region, confirming height similarity in both the streamwise and spanwise projections. A systematic displacement between the two columns is also evident and is consistent with the anisotropic cross-over scales ($\ell_y = R\,\ell_x$) implied by the planform geometry. At the smallest separations, departures from unit-slope alignment reflect the breakdown of the attached-eddy description as smaller-scale dynamics intervenes, whereas at the largest separations the contours flatten

https://doi.org/10.1017/jfm.2026.11692 Published online by Cambridge University Press

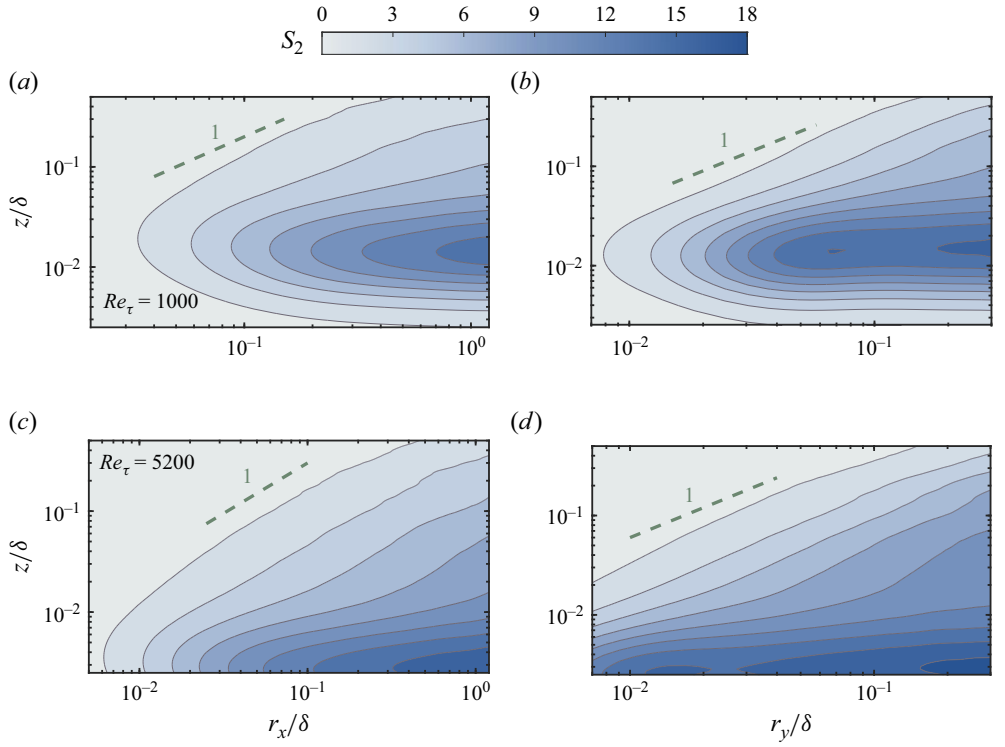


Figure 3. Contours of the 1-D projections of the equal-height second-order structure function in the $(r_i/\delta,\ z/\delta)$ plane (log–log axes): $S_2(r_x, 0; z)$ (left column) and $S_2(0, r_y; z)$ (right column). Panels (a, b) correspond to $Re_\tau = 1000$ and (c, d) to $Re_\tau = 5200$. The green dashed guides have unit slope and indicate $r_i \propto z$ (i.e. constant r_i/z), which is the expected organisation of iso-levels in the logarithmic branches of (3.9)–(3.10).

as the outer cutoff becomes active (see the plateau branches in (3.9)–(3.10)). Compared with $Re_\tau = 1000$, the $Re_\tau = 5200$ contours follow the $r_i/z = \text{const}$ organisation over a broader range of (r_i, z), consistent with the increased scale separation available at higher Reynolds number.

4.2. *Two-dimensional structure-function geometry and parameterisation*

We now examine the full equal-height field $S_2(r_x, r_y; z)$ and assess whether the elliptic closure captures the observed in-plane iso-level geometry without introducing additional degrees of freedom beyond those constrained by the 1-D projections.

Figure 4 compares the DNS iso-levels of $S_2(r_x, r_y; z)$ with the ellipses implied by (3.11) at $z/\delta = 0.10$. For each given Re_τ and z, the 2-D structure function $S_2(r_x, r_y; z)$ in the present study is computed from the corresponding wall-parallel velocity plane, using the statistical homogeneity in the streamwise and spanwise directions to perform spatial averaging over all available reference points within that plane. The dashed curves are constructed from the semi-axes determined from the 1-D projections at the same wall distance (figure 2). For the displayed levels $S_2 = 2$–6, the semi-axes a and b are obtained from the intercepts of the streamwise and spanwise 1-D projections, respectively, at the same contour level along the two principal directions, and are then substituted into (3.11) to construct the corresponding iso-ellipses. Thus, a and b here are not obtained by fitting the full 2-D DNS iso-contours, but are geometric quantities constrained independently by the 1-D projections. In both Reynolds-number cases, the predicted ellipses reproduce

https://doi.org/10.1017/jfm.2026.11692 Published online by Cambridge University Press

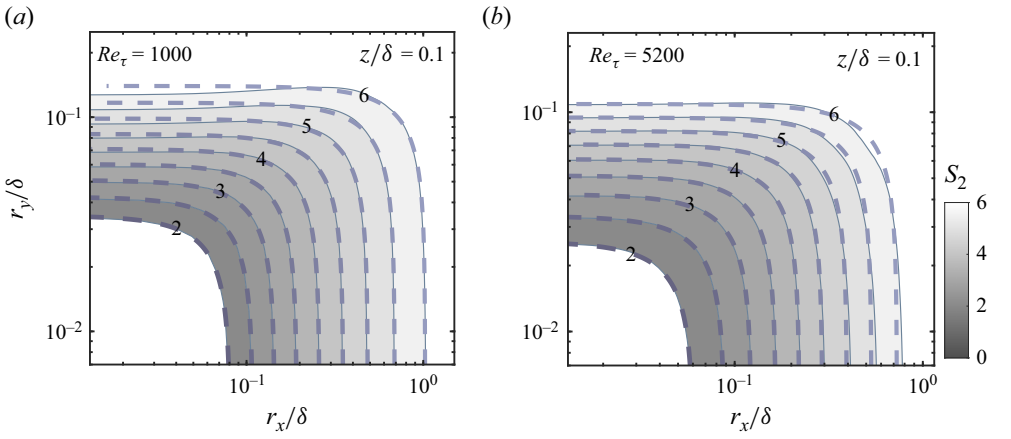


Figure 4. Equal-height 2-D structure function $S_2(r_x, r_y; z)$ at $z/\delta = 0.10$ for (*a*) $Re_\tau = 1000$ and (*b*) $Re_\tau = 5200$. Shaded contours show DNS iso-levels $S_2 = 2, 3, 4, 5, 6$. Dashed curves are the corresponding iso-ellipses obtained from (3.11), with the parameters inferred from the 1-D projections at the same z (figure 2) and with no additional tuning.

the DNS contours closely over the intermediate-separation range where the logarithmic branch is expected to apply, capturing both the in-plane anisotropy (relative stretching in r_x versus r_y) and the systematic spacing between successive levels.

Deviations are most apparent near the smallest separations, where the attached-eddy description underpinning the logarithmic branch is not expected to hold, and near the largest separations as the approach to the outer cutoff becomes influential (cf. the piecewise domains in (3.9)–(3.10) and the scope discussion in § 3.5). Importantly, the agreement in figure 4 is obtained without fitting the 2-D fields directly: parameters determined from the 1-D projections suffice to predict the off-axis geometry, supporting the consistency of the elliptic closure as a compact description of $S_2(r_x, r_y; z)$ in the logarithmic region.

Figure 5 summarises the geometry underlying the 2-D prediction in § 3. Within the HRAP counting argument, only eddies that are not shared by the two points contribute to the increment; the separation dependence enters solely through the shared-height mapping, which determines the effective upper limit of the logarithmic accumulation in (3.8). In the elliptic closure, this mapping produces self-similar elliptical iso-levels in the wall-parallel plane, with semi-axes that scale linearly with z at fixed level and with a z-independent aspect ratio $b/a = R$ (cf. (3.11)). The axis intercepts therefore reproduce the streamwise and spanwise 1-D limits and their cross-over scales (3.9)–(3.10). At sufficiently large separations the outer cutoff becomes active, leading to saturation towards the large-separation plateau predicted by (3.8), as indicated schematically by the flattening of the outermost contour.

In the elliptic closure, iso-levels in the (r_x, r_y) plane are parameterised by the semi-axes a and b (see (3.11)). A direct consequence is that, for fixed level $D^\star$ within the logarithmic branch, the normalised axes a/z and b/z are predicted to be independent of z (cf. (3.13)), while the aspect ratio b/a is set by the anisotropy parameter.

Figure 6(*a*, *b*) evaluates these predictions at $D^\star = 2$. Both a/z and b/z exhibit clear plateaux within the logarithmic windows, supporting the expected height self-similarity of the iso-level geometry at fixed level. The window-averaged values read $\langle a/z \rangle \simeq 0.78$ and 0.60, and $\langle b/z \rangle \simeq 0.34$ and 0.26 for $Re_\tau = 1000$ and 5200, respectively (horizontal lines). The triangles denote axis intercepts inferred independently from the corresponding

https://doi.org/10.1017/jfm.2026.11692 Published online by Cambridge University Press

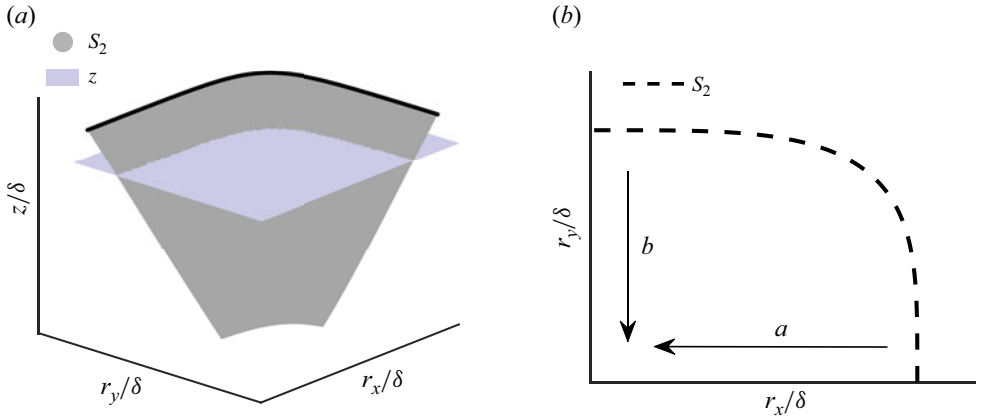


Figure 5. Schematic of the elliptic closure for the equal-height structure function. (*a*) Conceptual level surface of S_2 (grey) in the space $(r_x/\delta, r_y/\delta, z/\delta)$, intersected by a horizontal plane at fixed z (purple). (*b*) Plan view of the intersection in the (r_x, r_y) plane, which is an ellipse with semi-axes a and b. For a prescribed level $D^\star$ in the intermediate range, (3.11) gives $(r_x/a)^2 + (r_y/b)^2 = 1$ with $b/a = R$, and the intercepts on the coordinate axes recover the 1-D reductions (3.9)–(3.10). The gradual flattening of the dashed contour at large r_i/δ indicates the onset of the outer cutoff, i.e. the approach to the plateau enforced by (3.8).

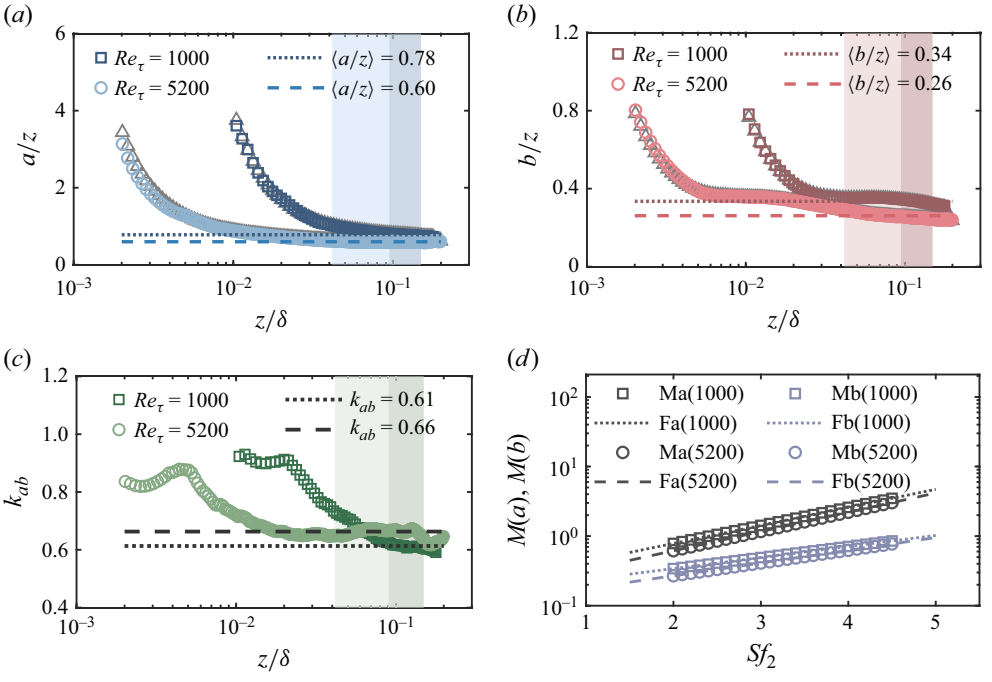


Figure 6. Ellipse metrics extracted from iso-levels of the equal-height structure function. (*a*) Streamwise semi-axis a normalised by z at the level $D^\star = 2$ versus z/δ; (*b*) spanwise semi-axis b/z at $D^\star = 2$ versus z/δ. Squares: $Re_\tau = 1000$; circles: $Re_\tau = 5200$. Shaded bands indicate the logarithmic-region windows used for averaging: $0.095 < z/\delta < 0.15$ for $Re_\tau = 1000$ and $0.0416 < z/\delta < 0.15$ for $Re_\tau = 5200$; horizontal lines show the corresponding window means. (*c*) Coupling between departures of a/z and b/z quantified by $k_{ab}(z) \equiv \mathrm{d}\ln(b/z)/\mathrm{d}\ln(a/z)$; dotted/dashed lines denote window-averaged values over the same intervals. (*d*) Window-averaged axes $M(a) \equiv \langle a/z\rangle$ and $M(b) \equiv \langle b/z\rangle$ as functions of level $D^\star$, together with least-squares fits of (4.2) (labelled F_a and F_b). Triangles in (a, b) indicate the corresponding axis intercepts inferred independently from the 1-D projections at the same level.

https://doi.org/10.1017/jfm.2026.11692 Published online by Cambridge University Press

Re_τ	C_{a1}	C_{a2}	C_{b1}	C_{b2}
1000	0.259	−0.624	0.159	−0.785
5200	0.276	−0.763	0.183	−0.936

Table 1. Coefficients of the base-10 fits (4.2) obtained over the logarithmic-region windows used in figure 6. Here, $D^\star$ is a contour level of the dimensionless structure function S_2, and $M(a) = \langle a/z \rangle$ and $M(b) = \langle b/z \rangle$ are also dimensionless quantities; therefore, C_{a1}, C_{a2}, C_{b1} and C_{b2} are all dimensionless coefficients. In the ideal asymptote, one would expect equal slopes $C_{a1} = C_{b1} = 1/(2A_1 \ln 10)$ and an offset $C_{b2} - C_{a2} = \log_{10}(b/a)$; departures quantify finite-Re_τ effects in the extracted axis ratios.

1-D projections at the same level; their close agreement with the 2-D extraction indicates that the in-plane geometry is consistent with the 1-D constraints.

To quantify how the residual z-dependence of a/z and b/z is coupled, we introduce the local log–log slope

$$k_{ab}(z) \equiv \frac{\mathrm{d}\ln(b/z)}{\mathrm{d}\ln(a/z)}. \tag{4.1}$$

If the aspect ratio were strictly z-independent, $\ln(b/z) = \ln(a/z) + \ln(b/a)$ would imply $k_{ab} = 1$. Figure 6(*c*), however, shows that k_{ab} attains nearly constant values within the logarithmic windows, with averages $\langle k_{ab} \rangle \simeq 0.61$ for $Re_\tau = 1000$ and $\simeq 0.66$ for $Re_\tau = 5200$. The systematic deviation from unity quantifies a weak finite-Re_τ drift in the observed axis ratio across the available overlap region; this is consistent with the limited scale separation and the proximity of the fitting windows to the neighbouring ranges. It should therefore be interpreted as a pre-asymptotic finite-Re_τ effect over the present DNS range, rather than as direct evidence against the ideal AEEA closure.

Finally, (3.11) implies an exponential dependence of the (window-averaged) semi-axes on the level $D^\star$. Defining $M(a) \equiv \langle a/z \rangle$ and $M(b) \equiv \langle b/z \rangle$ as window-averaged quantities at fixed Re_τ, the ideal prediction is that $M(a)$ and $M(b)$ vary linearly with $D^\star$ when plotted on a logarithmic ordinate. In the base-10 representation used in figure 6(*d*), we fit

$$\log_{10} M(a) = C_{a1}\, D^\star + C_{a2}, \qquad \log_{10} M(b) = C_{b1}\, D^\star + C_{b2}, \tag{4.2}$$

over the range $D^\star \in [2, 6]$. Here, C_{a1}, C_{a2}, C_{b1}, C_{b2} are empirical regression coefficients that characterise the dependence of the DNS-extracted semi-axes on the level $D^\star$, and provide a compact representation of this level dependence at finite Re_τ. The fitted lines (F_a, F_b) follow the DNS trends closely, indicating that this parsimonious parameterisation captures the variation of the semi-axes with level while remaining consistent with the 1-D constraints. Accordingly, at fixed wall-normal height, the family of 2-D iso-level contours can be represented in a unified manner by these geometric parameters, rather than being extracted contour by contour from the full 2-D field.

Combining (4.2) with the fitted coefficients in table 1 yields the semi-axis parameterisation

$$a(z;\, D^\star) = z\, 10^{\,C_{a1}\, D^\star + C_{a2}}, \tag{4.3a}$$

$$b(z;\, D^\star) = z\, 10^{\,C_{b1}\, D^\star + C_{b2}}, \tag{4.3b}$$

which encodes the approximately linear-in-z dilation of iso-level sets in the logarithmic region and the observed exponential dependence of the (window-averaged) axes on the level $D^\star$.

The fits in figure 6(*d*) and table 1 provide a compact representation of the level dependence of the ellipse semi-axes via (4.3*a*)–(4.3*b*). For any prescribed level $D^\star$ and

https://doi.org/10.1017/jfm.2026.11692 Published online by Cambridge University Press

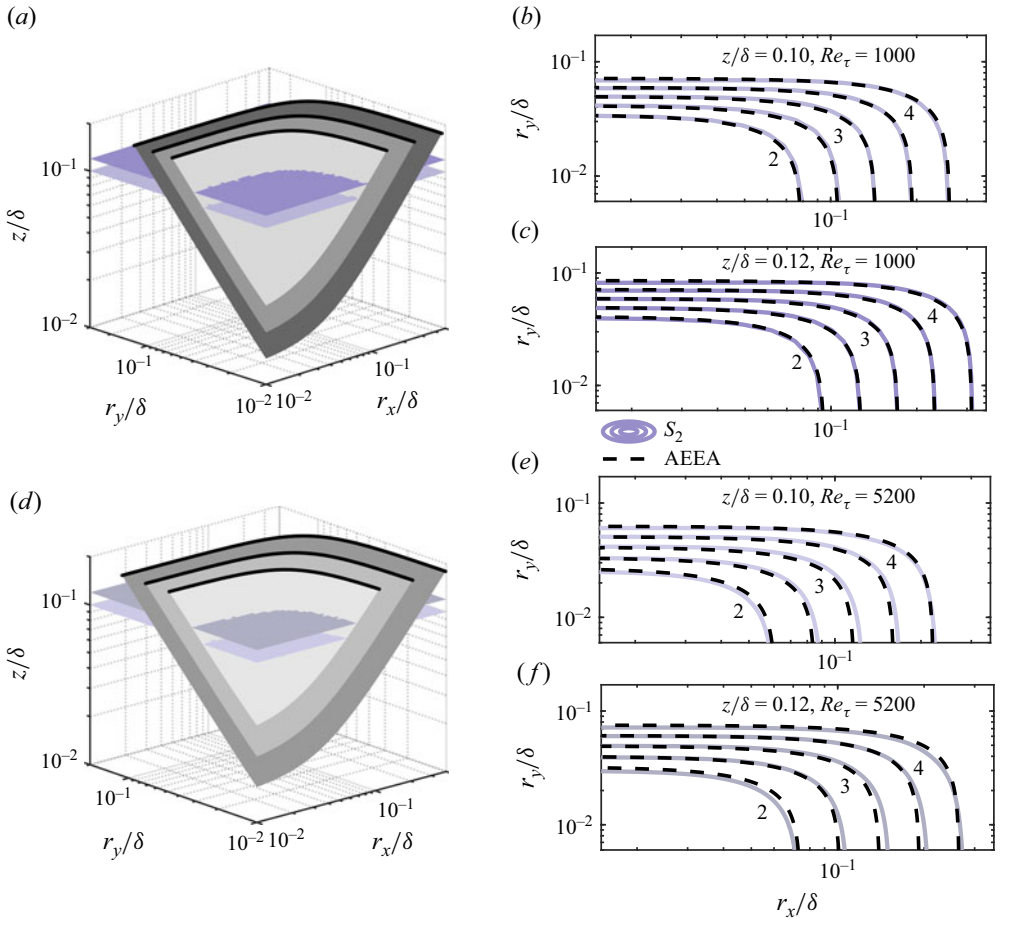


Figure 7. Validation of the elliptic closure using the parameterised semi-axes. (*a*, *d*) Predicted iso-surfaces of the equal-height structure function at levels $D^\star = 2, 3, 4$ (grey shades; darker indicates larger $D^\star$) for $Re_\tau = 1000$ and 5200, respectively. The surfaces are constructed by combining the fitted semi-axes (4.3*a*)–(4.3*b*) with the elliptic level-set relation in (3.11). Semi-transparent purple planes mark the slice heights $z/\delta = 0.10$ and 0.12. (*b*, *c*, *e*, *f*) Wall-parallel slices at the indicated heights: DNS iso-contours at $D^\star = 2, 3, 4$ are shown in purple, and the corresponding predictions are shown as black dashed ellipses.

wall distance z within the logarithmic region, these expressions specify the ellipse size, which can then be combined with the elliptic level-set relation in (3.11) to generate predicted iso-contours and iso-surfaces.

Figure 7 assesses this parameterised prediction against DNS. The top row shows the reconstructed iso-surfaces at $D^\star = 2, 3, 4$, together with two representative wall-parallel slices at $z/\delta = 0.10$ and 0.12. The corresponding slices are shown in panels (*b*, *c*, *e*, *f*), where DNS iso-contours are compared directly with the predicted ellipses. Across both Reynolds numbers and both slice heights, the parameterised ellipses reproduce the DNS contour sizes and anisotropic shapes closely over the intermediate separations relevant to the logarithmic branch. The remaining mismatches are most noticeable towards the largest separations, consistent with the progressive influence of the outer cutoff, and towards the smallest separations where the attached-eddy description is not expected to apply.

For the wall-parallel slices in figure 7, we further quantify the agreement between the predicted ellipses and the DNS iso-contours. Owing to symmetry with respect to both

https://doi.org/10.1017/jfm.2026.11692 Published online by Cambridge University Press

z/δ	$D^\star$	$Re_\tau = 1000$			$Re_\tau = 5200$		
		$E_{r,mean}$	$E_{r,max}$	IoU	$E_{r,mean}$	$E_{r,max}$	IoU
0.10	2	0.0164	0.0206	0.674	0.0355	0.0427	0.610
0.10	3	0.0189	0.0301	0.794	0.0362	0.0570	0.763
0.10	4	0.0122	0.0359	0.866	0.0174	0.0329	0.860
0.12	2	0.0090	0.0191	0.718	0.0518	0.0657	0.643
0.12	3	0.0114	0.0224	0.829	0.0232	0.0666	0.803
0.12	4	0.0160	0.0420	0.885	0.0366	0.0464	0.846

Table 2. Quantitative comparison between the parameterised elliptic prediction and the DNS iso-contours at the representative contour levels $D^\star = 2, 3, 4$. The error metrics are reported for two representative wall distances, $z/\delta \approx 0.10$ and 0.12, and for both Reynolds numbers. Here, $E_{r,mean}$ and $E_{r,max}$ denote the mean and maximum normalised radial deviations, and IoU is the area-overlap ratio in the first quadrant.

coordinate axes, the comparison is restricted to the first quadrant. Let $\phi \in [0, \pi/2]$ denote the polar angle in the (r_x, r_y) plane, and let $r_{DNS}(\phi; D^\star, z)$ and $r_{pred}(\phi; D^\star, z)$ denote the radial positions of the DNS iso-contour and the predicted ellipse, respectively, at wall distance z and contour level $D^\star$. We define the mean normalised radial deviation as

$$E_{r,mean}(D^\star, z) = \frac{2}{\pi} \int_0^{\pi/2} \frac{|r_{DNS}(\phi; D^\star, z) - r_{pred}(\phi; D^\star, z)|}{r_{DNS}(\phi; D^\star, z)} \, \mathrm{d}\phi, \tag{4.4}$$

and the maximum normalised radial deviation as

$$E_{r,max}(D^\star, z) = \max_{\phi \in [0,\pi/2]} \frac{|r_{DNS}(\phi; D^\star, z) - r_{pred}(\phi; D^\star, z)|}{r_{DNS}(\phi; D^\star, z)}. \tag{4.5}$$

In addition, letting $A_{DNS}(D^\star, z)$ and $A_{pred}(D^\star, z)$ denote the enclosed regions of the DNS iso-contour and the predicted ellipse in the first quadrant, respectively, we define the area-overlap ratio by

$$\mathrm{IoU}(D^\star, z) = \frac{|A_{DNS}(D^\star, z) \cap A_{pred}(D^\star, z)|}{|A_{DNS}(D^\star, z) \cup A_{pred}(D^\star, z)|}. \tag{4.6}$$

Thus, smaller values of $E_{r,mean}$ and $E_{r,max}$ indicate closer contour agreement, whereas a larger IoU indicates better overall geometric overlap. Table 2 reports these metrics for the representative contour levels $D^\star = 2, 3, 4$ at the two wall heights and Reynolds numbers considered here.

The results in table 2 are broadly consistent with the visual comparison in figure 7. Across the cases considered, $E_{r,mean}$ lies in the range 0.009–0.052, while IoU ranges from 0.61 to 0.89. In particular, for the intermediate and higher levels $D^\star = 3$ and 4, the mean radial deviation typically remains within approximately 1 %–4 %, while the area-overlap ratio is mostly in the range 0.76–0.89, indicating that the parameterised ellipses capture both the contour size and the anisotropic in-plane geometry with good fidelity. By contrast, the agreement is somewhat weaker at the lowest level, which is consistent with the increased sensitivity of these contours to the edge of the model applicability range, including both the small-separation side and the onset of the outer cutoff. Overall, figure 7 and table 2 together show that the 2-D organisation of $S_2(r_x, r_y; z)$ can be represented reliably by an elliptic geometry whose semi-axes are constrained by the 1-D projections and summarised by the parsimonious fits (4.3*a*)–(4.3*b*). Because the DNS structure functions reported here are not further averaged over multiple temporal snapshots, the extracted contours and the associated error metrics may retain some residual sampling uncertainty, especially at large separations where the number of effectively independent

https://doi.org/10.1017/jfm.2026.11692 Published online by Cambridge University Press

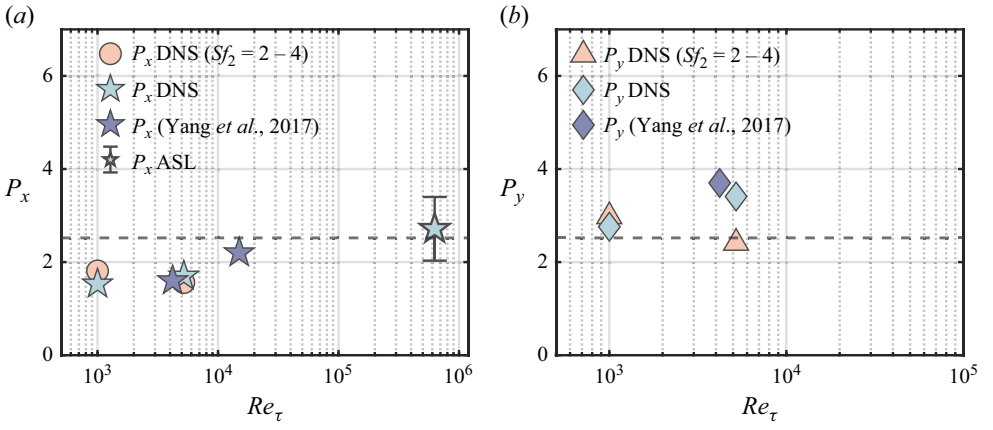


Figure 8. Effective logarithmic slopes extracted from the 1-D projections of the equal-height structure function. (*a*) Streamwise coefficient P_x versus Re_τ; (*b*) spanwise coefficient P_y versus Re_τ. The DNS slopes obtained from least-squares fits of S_2 against $\ln(r_i/z)$ using a fixed-level window $D^\star \in [2, 4]$ are shown by circles in (*a*) and triangles in (*b*). The DNS fits over the geometric window $1 < r_i/z < 10$ are shown by stars in (*a*) and diamonds in (*b*). Dark markers reproduce the compilation of Yang *et al.* (2017) over the same geometric window; the black star with error bar in (*a*) is an atmospheric surface-layer estimate over $1 < r_x/z < 10$. The horizontal dashed line indicates the asymptotic slope $P = 2A_1$ implied by the attached-eddy counting argument in the logarithmic branch (see § 3).

samples is reduced. More generally, the extracted semi-axes, effective logarithmic slopes and finite-Re_τ diagnostics should be interpreted as effective estimates for the present DNS datasets and analysis windows, since their numerical values may also depend on the contour-extraction procedure and the choice of fitting windows.

Figure 8 summarises effective logarithmic slopes obtained from the 1-D projections of the equal-height structure function in the logarithmic branch. In practice, P_x and P_y are extracted from least-squares fits of S_2 versus $\ln(r_i/z)$ using two complementary choices of fitting window: a fixed-level window $D^\star \in [2, 4]$, which targets the intermediate-range portion emphasised in figures 2–7, and a geometric window $1 < r_i/z < 10$, which enables direct comparison with the compilation of Yang *et al.* (2017) and the atmospheric estimate shown in panel (*a*). The latter is introduced not as a replacement for the fixed-level definition used above, but as a unified comparison window across datasets and as a supplementary check on the sensitivity of the inferred slopes to the fitting-window definition. The dashed line indicates the asymptotic slope $P = 2A_1 = 2.5$ expected from the attached-eddy counting argument within the logarithmic branch.

In the streamwise direction (figure 8*a*), the fitted values of P_x over the presently available DNS Reynolds-number range remain below the asymptotic reference, but the results obtained from the two fitting windows are close to each other, indicating only a weak sensitivity of the streamwise estimates to the fitting-window definition. The compilation point from Yang *et al.* (2017) at higher Re_τ, together with the atmospheric estimate, lies closer to the asymptotic reference, consistent with a gradual approach towards the common slope as the overlap region broadens. This behaviour is consistent with the more restrictive streamwise admissible interval associated with the cross-over and outer cap in the piecewise 1-D reductions (cf. (3.9)).

In the spanwise direction (figure 8*b*), the extracted slopes are systematically larger than their streamwise counterparts at comparable Re_τ. Compared with the streamwise case, the results obtained from the two fitting windows exhibit a clearer difference at $Re_\tau = 5200$, indicating that, within the present DNS range, the sensitivity of the spanwise estimates

https://doi.org/10.1017/jfm.2026.11692 Published online by Cambridge University Press

to the fitting-window definition becomes more visible at the higher Reynolds number. The comparison with Yang *et al.* (2017) shows that this directional disparity persists at moderately higher Re_τ, indicating that the currently accessible Reynolds numbers are not yet fully in the asymptotic regime where the attached-eddy picture would yield a common slope in the logarithmic branch. Therefore, the extracted values of P_x and P_y should be interpreted as effective logarithmic slopes obtained over the presently accessible fitting windows; their departures from the common asymptotic slope $2A_1$ may be understood as pre-asymptotic deviations at finite Re_τ, rather than as evidence against the common-slope picture itself. This interpretation is also consistent with the cautious discussion of directional differences in effective slopes within the HRAP framework by Yang *et al.* (2017). Overall, figure 8 therefore quantifies the finite-Re_τ and direction-dependent departures from the asymptotic prediction, while remaining consistent with the trend that increasing scale separation reduces the dependence of the inferred slopes on the fitting protocol.

4.3. *Unified relation among geometric coupling, regression coefficients and directional slopes*

This subsection relates three quantities extracted independently in § 4.1–§ 4.2: (i) the geometric coupling between the semi-axes of the iso-S_2 sets, (ii) the slopes of the level-axis regressions for the window-averaged intercepts and (iii) the effective logarithmic slopes obtained from the 1-D projections. Within a common logarithmic window, these diagnostics quantify the same anisotropic dilation of the equal-height level sets.

Consider an iso-level $S_2 = D^\star$ at fixed z within the logarithmic branch. Its intercepts with the coordinate axes define the semi-axes a and b. From the 1-D logarithmic forms in (3.9)–(3.10), the dependence of the normalised intercepts on the level satisfies

$$\frac{\mathrm{d}\ln(a/z)}{\mathrm{d}D^\star} = \frac{1}{P_x}, \qquad \frac{\mathrm{d}\ln(b/z)}{\mathrm{d}D^\star} = \frac{1}{P_y}, \tag{4.7}$$

where P_x and P_y are the effective slopes extracted from S_2 versus $\ln(r_i/z)$ in the streamwise and spanwise directions, respectively, using the same fitting window.

Next, define the window-averaged intercepts $M(a) \equiv \langle a/z \rangle$ and $M(b) \equiv \langle b/z \rangle$ (cf. figure 6*d*). The empirical base-10 regressions (4.2) imply, upon differentiation,

$$\frac{\mathrm{d}\ln M(a)}{\mathrm{d}D^\star} = (\ln 10)\, C_{a1}, \qquad \frac{\mathrm{d}\ln M(b)}{\mathrm{d}D^\star} = (\ln 10)\, C_{b1}, \tag{4.8}$$

so that the ratio of regression slopes measures the relative sensitivity of $M(a)$ and $M(b)$ to the level

$$\frac{C_{a1}}{C_{b1}} = \frac{\mathrm{d}\ln M(a)/\mathrm{d}D^\star}{\mathrm{d}\ln M(b)/\mathrm{d}D^\star}. \tag{4.9}$$

Comparing (4.7) and (4.8) within the same logarithmic window yields the approximate correspondence

$$\frac{C_{a1}}{C_{b1}} \approx \frac{(1/P_x)}{(1/P_y)} = \frac{P_y}{P_x}, \tag{4.10}$$

where the approximation reflects the fact that $M(\cdot)$ involves an additional averaging over z (and, in practice, finite-Re_τ departures from perfect overlap).

Finally, recall the geometric coupling introduced in (4.1)

$$k_{ab}(z) \equiv \frac{\mathrm{d}\ln(b/z)}{\mathrm{d}\ln(a/z)}. \tag{4.11}$$

https://doi.org/10.1017/jfm.2026.11692 Published online by Cambridge University Press

Evaluating this derivative along increasing level $D^\star$ (at fixed z) and applying the chain rule gives

$$k_{ab} = \frac{\mathrm{d}\ln(b/z)/\mathrm{d}D^\star}{\mathrm{d}\ln(a/z)/\mathrm{d}D^\star} \approx \frac{C_{b1}}{C_{a1}} \approx \frac{P_x}{P_y}. \tag{4.12}$$

Equation (4.12) shows that the anisotropic dilation of the equal-height iso-S_2 sets (quantified by k_{ab}), the level-axis regression slopes (C_{a1}, C_{b1}), and the directional 1-D slopes (P_x, P_y) provide mutually consistent measures of the same effect within a common logarithmic window. In the ideal asymptotic limit where the directional slopes coincide ($P_x \to P_y$), one expects $k_{ab} \to 1$, corresponding to level sets that dilate isotropically in the logarithmic scaling (i.e. a z-independent aspect ratio in the strict elliptic closure). At the present Reynolds numbers, deviations from unity quantify finite-Re_τ departures from the asymptotic regime discussed in § 4.1–§ 4.2.

5. Conclusion

Motivated by Townsend's AEH and its HRAP interpretation, we proposed AEEA as an elliptic closure for the equal-height 2-D second-order structure function in the logarithmic region. The core of this closure is to write the shared-eddy condition in the wall-parallel 2-D structure function explicitly as a level-set geometry in the wall-parallel plane. On the basis of this representation, the resulting AEEA provides a closed prediction for $S_2(r_x, r_y; z)$, in which the level sets in the intermediate-separation range form a self-similar family of ellipses. The underlying theoretical closure of the model is parameterised by four quantities (A_1, C_{11}, θ, R): $2A_1$ sets the logarithmic slope of the 1-D projections, C_{11} fixes the additive offset, θ controls the cross-over scale through the mapping between in-plane separation and shared-eddy height and R governs the in-plane anisotropy of the level-set geometry.

Direct numerical simulations of turbulent channel flow at $Re_\tau = 1000$ and 5200 support the model in three principal respects. First, the 1-D projections exhibit height similarity when plotted versus r_i/z ($i = x, y$), and show an approximately linear dependence of S_2 on $\ln(r_i/z)$ over an intermediate window, consistent with the logarithmic branch predicted by the attached-eddy counting argument. Second, contours in $(r_i/\delta, z/\delta)$ align approximately with $r_i \propto z$ within the logarithmic layer, providing a geometric expression of the same height similarity. Third, at fixed z, iso-levels in the (r_x, r_y) plane are accurately represented by ellipses whose sizes and aspect ratios are captured using parameters inferred from the 1-D projections, without additional tuning, indicating that a single pair (θ, R) provides an effective description of wall-parallel anisotropy over the intermediate separations considered.

The dilation with height and level was quantified by extracting the semi-axes (a, b) of the iso-S_2 sets at prescribed levels $D^\star$. Within logarithmic-region windows, both a/z and b/z exhibit clear plateaux, consistent with z-self-similar level-set geometry. The associated coupling $k_{ab} = \mathrm{d}\ln(b/z)/\mathrm{d}\ln(a/z)$ remains approximately constant within the same windows; deviations from the asymptotic value unity quantify finite-Re_τ departures from the idealised overlap. Moreover, the window-averaged semi-axes vary approximately exponentially with $D^\star$, yielding a compact parameterisation of the level-set geometry,

$$a(z;\, D^\star) = z\, 10^{\,C_{a1}D^\star + C_{a2}}, \qquad b(z;\, D^\star) = z\, 10^{\,C_{b1}D^\star + C_{b2}}, \tag{5.1}$$

which reconstructs the DNS iso-levels with high fidelity over the intermediate range of levels considered. The effective 1-D slopes show a mild directional and Reynolds-number dependence: spanwise estimates are comparatively stable across the present Reynolds

https://doi.org/10.1017/jfm.2026.11692 Published online by Cambridge University Press

numbers, whereas streamwise estimates exhibit a stronger finite-Re_τ sensitivity, consistent with the more restrictive streamwise overlap available at moderate Re_τ.

Overall, the AEEA provides a geometrically transparent and quantitatively predictive framework for the 2-D organisation of equal-height structure functions in the logarithmic region. It recovers the established 1-D logarithmic laws and height similarity, and it supplies a parsimonious parameterisation for the wall-parallel level-set geometry that is directly constrained by the 1-D projections. The remaining discrepancies with the asymptotic idealisation (e.g. $k_{ab} \neq 1$ and $P_x \neq P_y$ within the present DNS range) are consistent with finite-Re_τ effects and the limited breadth of the overlap. In this sense, these departures should be interpreted as pre-asymptotic deviations at finite Re_τ, while the recovery of a common logarithmic slope and an approximately z-independent level-set aspect ratio at sufficiently high Reynolds number should still be viewed as the asymptotic expectation. The present framework provides a natural starting point for extension to other structure-function components, but such extensions apply most directly to cases that also exhibit logarithmic branches along the principal directions. For components such as the wall-normal one, whose logarithmic-region behaviour follows a different type of scaling, a treatment different from the present AEEA would be required. Extensions to non-equal-height statistics and to composite descriptions incorporating inertial- and viscous-range behaviour at sufficiently small separations may also be pursued on this basis.

Acknowledgements. The authors acknowledge the Fluid Mechanics Research Group at the University of Melbourne for providing public access to the database. The authors thank Ivan Marusic, Nicholas Hutchins, Woutijn J. Baars, and Dominik Krug for their assistance in accessing the raw datasets. The authors also thank M. Lee and R. Moser for making the channel flow database publicly available.

Funding. This work was supported by the Youth Project of the Science and Technology Research Program of Chongqing Municipal Education Commission of China (KJQN202501148), the National Natural Science Foundation of China (No. 12402251), and the Natural Science Foundation of Chongqing (CSTB2025NSCQ-GPX0969).

Declaration of interests. The authors report no conflict of interest.

Appendix A. A spectral route to the two-dimensional second-order structure function

This appendix summarises an efficient spectral route for evaluating the equal-height, wall-parallel second-order structure function on a plane at fixed wall-normal position z. The procedure avoids explicit pairwise accumulation in physical space and is particularly convenient for uniformly sampled periodic planes, as in DNS.

Let $u(\boldsymbol{x})$ denote a scalar field (or a single velocity component) defined on a wall-parallel plane, with $\boldsymbol{x} = (x, y)$. After removing the plane mean, the equal-height 2-D second-order structure function is

$$S_2(\boldsymbol{r}) \equiv \left\langle [u(\boldsymbol{x}+\boldsymbol{r}) - u(\boldsymbol{x})]^2 \right\rangle, \qquad \boldsymbol{r} = (r_x, r_y), \tag{A1}$$

where $\langle\cdot\rangle$ denotes an average over (x, y) (and time, if multiple snapshots are available). Under in-plane homogeneity, S_2 depends only on $\boldsymbol{r}$.

A.1. *Identity in terms of the autocovariance and spectral density*

Expanding (A1) and invoking homogeneity yields the standard identity

$$S_2(\boldsymbol{r}) = 2\left(\langle u^2 \rangle - R_{uu}(\boldsymbol{r})\right), \tag{A2}$$

https://doi.org/10.1017/jfm.2026.11692 Published online by Cambridge University Press

where

$$R_{uu}(\boldsymbol{r}) \equiv \langle u(\boldsymbol{x})\, u(\boldsymbol{x}+\boldsymbol{r})\rangle \tag{A3}$$

is the in-plane autocovariance. For a homogeneous field, R_{uu} is related to the (2-D) power spectral density $\Phi_{uu}(\boldsymbol{k})$ by the Wiener–Khinchin theorem. In continuous form

$$R_{uu}(\boldsymbol{r}) = \iint \Phi_{uu}(\boldsymbol{k})\, \mathrm{e}^{\,i\boldsymbol{k}\cdot\boldsymbol{r}}\, \mathrm{d}\boldsymbol{k}, \qquad \boldsymbol{k} = (k_x, k_y). \tag{A4}$$

Substituting (A4) into (A2) gives the spectral representation

$$S_2(\boldsymbol{r}) = 2\iint \Phi_{uu}(\boldsymbol{k})[1-\cos(\boldsymbol{k}\cdot\boldsymbol{r})]\, \mathrm{d}\boldsymbol{k} = 4\iint \Phi_{uu}(\boldsymbol{k})\, \sin^2\!\left(\tfrac{\boldsymbol{k}\cdot\boldsymbol{r}}{2}\right) \mathrm{d}\boldsymbol{k}. \tag{A5}$$

Equation (A5) emphasises the scale-selective weighting: modes that remain nearly in phase over $\boldsymbol{r}$ contribute weakly, whereas out-of-phase modes contribute strongly. One-dimensional projections follow by setting $r_y = 0$ or $r_x = 0$.

A.2. *Discrete implementation for periodic DNS planes*

For the periodic planes typical of channel-flow DNS, the practical computation is most naturally expressed in discrete form. Let $u_{mn} = u(x_m, y_n)$ be sampled on an $N_x \times N_y$ uniform grid. Denote the discrete Fourier transform by $\widehat{u}_{pq}$ and the corresponding discrete wavenumbers by $(k_{x,p}, k_{y,q})$. Parseval-consistent normalisation is assumed.

The autocovariance on the periodic domain is obtained by a single inverse fast Fourier transform (IFFT) of the power spectrum

$$R_{uu}\big(r_{x,i}, r_{y,j}\big) = \mathrm{IFFT}\left(|\widehat{u}_{pq}|^2\right), \tag{A6}$$

where $(r_{x,i}, r_{y,j})$ are the discrete lags implied by the grid and periodicity. The structure function is then recovered pointwise via (A2):

$$S_2(r_{x,i}, r_{y,j}) = 2\big(R_{uu}(0,0) - R_{uu}\big(r_{x,i}, r_{y,j}\big)\big). \tag{A7}$$

This route reduces the computational cost from $O(N_x^2 N_y^2)$ for explicit pairwise accumulation to $O(N_x N_y \log(N_x N_y))$ for one fast Fourier transform (FFT)/IFFT pair, while preserving energy consistency (in particular, $R_{uu}(0,0) = \langle u^2\rangle$ and $S_2(0,0) = 0$). The full directional dependence in (r_x, r_y) is retained, which is essential for anisotropic wall-bounded flows.

A.3. *Limits and practical remarks*

At sufficiently small separations, if u is smooth

$$S_2(\boldsymbol{r}) \sim \left\langle |\nabla u|^2 \right\rangle |\boldsymbol{r}|^2, \qquad |\boldsymbol{r}| \to 0, \tag{A8}$$

whereas in an inertial subrange of (locally) isotropic turbulence

$$S_2(\boldsymbol{r}) \sim C_2\big(\varepsilon\, |\boldsymbol{r}|\big)^{2/3}. \tag{A9}$$

These asymptotic forms are quoted for general context; the present work focuses on the intermediate, energy-containing logarithmic branch discussed in § 3. For large separations, decorrelation implies

$$S_2(\boldsymbol{r}) \to 2\langle u^2\rangle, \qquad |\boldsymbol{r}| \text{ large}, \tag{A10}$$

consistent with the plateau underlying the attached-eddy-based descriptions.

https://doi.org/10.1017/jfm.2026.11692 Published online by Cambridge University Press

In practice, it is advisable to (i) remove the plane mean prior to the FFT; (ii) recognise that (A6) yields the periodic autocovariance appropriate to DNS boxes; and (iii) for non-periodic sub-windows (e.g. cropped experimental fields), apply tapering and/or zero padding to mitigate wrap-around artefacts. With a consistent normalisation, (A6)–(A7) provide a transparent and efficient route to $S_2(r_x, r_y)$ that retains full directional fidelity for comparisons with the attached-eddy predictions.

References

ADRIAN, R.J. 2007 Hairpin vortex organization in wall turbulence. *Phys. Fluids* **19** (4), 041301.

DEL ÁLAMO, J.C., JIMÉNEZ, J., ZANDONADE, P. & D MOSER, R. 2004 Scaling of the energy spectra of turbulent channels. *J. Fluid Mech.* **500**, 135.

BAARS, W.J., HUTCHINS, N. & MARUSIC, I. 2017 Self-similarity of wall-attached turbulence in boundary layers. *J. Fluid Mech.* **823**, R2.

BAARS, W.J. & MARUSIC, I. 2020 Data-driven decomposition of the streamwise turbulence kinetic energy in boundary layers. Part 2. Integrated energy and a_1. *J. Fluid Mech.* **882**, A26.

CASCIOLA, C.M., GUALTIERI, P., BENZI, R. & PIVA, R. 2003 Scale-by-scale budget and similarity laws for shear turbulence. *J. Fluid Mech.* **476**, 105–114.

CHANDRAN, D., BAIDYA, R., MONTY, J.P. & MARUSIC, I. 2017 Two-dimensional energy spectra in high-Reynolds-number turbulent boundary layers. *J. Fluid Mech.* **826**, R1.

CHAUHAN, K., HUTCHINS, N., MONTY, J. & MARUSIC, I. 2013 Structure inclination angles in the convective atmospheric surface layer. *Boundary-Layer Meteorol.* **147**, 41–50.

CIMARELLI, A., DE ANGELIS, E., JIMÉNEZ, J. & CASCIOLA, C.M. 2016 Cascades and wall-normal fluxes in turbulent channel flows. *J. Fluid Mech.* **796**, 417–436.

DAVIDSON, P.A. & KROGSTAD, P.-Å. 2009 A simple model for the streamwise fluctuations in the log-law region of a boundary layer. *Phys. Fluids* **21** (5), 055105.

DAVIDSON, P.A. & KROGSTAD, P.-Å. 2014 A universal scaling for low-order structure functions in the log-law region of smooth-and rough-wall boundary layers. *J. Fluid Mech.* **752**, 140–156.

DAVIDSON, P.A., KROGSTAD, P.-Å. & NICKELS, T.B. 2006*a* A refined interpretation of the logarithmic structure function law in wall layer turbulence. *Phys. Fluids* **18** (6), 065112.

DAVIDSON, P.A., NICKELS, T.B. & KROGSTAD, P-Å 2006*b* The logarithmic structure function law in wall-layer turbulence. *J. Fluid Mech.* **550**, 51–60.

DE SILVA, C.M., MARUSIC, I., WOODCOCK, J.D. & MENEVEAU, C. 2015 Scaling of second-and higher-order structure functions in turbulent boundary layers. *J. Fluid Mech.* **769**, 654–686.

FAVRE, A.J., GAVIGLIO, J.J. & DUMAS, R.J. 1958 Further space-time correlations of velocity in a turbulent boundary layer. *J. Fluid Mech.* **3** (4), 344–356.

FRISCH, U. & KOLMOGOROV, A.N. 1995 *Turbulence: the Legacy of AN Kolmogorov*. Cambridge University Press.

GRAHAM, J. 2016 A web services accessible database of turbulent channel flow and its use for testing a new integral wall model for LES. *J. Turbul.* **17** (2), 181–215.

HE, G., JIN, G. & YANG, Y. 2017 Space-time correlations and dynamic coupling in turbulent flows. *Annu. Rev. Fluid Mech.* **49** (1), 51–70.

HE, G.-W. & ZHANG, J.-B. 2006 Elliptic model for space-time correlations in turbulent shear flows. *Phys. Rev. E—Stat. Nonlinear Soft Matt. Phys.* **73** (5), 055303.

HILL, R.J. 2002 Exact second-order structure–function relationships. *J. Fluid Mech.* **468**, 317–326.

HULTMARK, M. 2012 A theory for the streamwise turbulent fluctuations in high Reynolds number pipe flow. *J. Fluid Mech.* **707**, 575–584.

HUTCHINS, N., CHAUHAN, K., MARUSIC, I., MONTY, J. & KLEWICKI, J. 2012 Towards reconciling the large-scale structure of turbulent boundary layers in the atmosphere and laboratory. *Boundary-Layer Meteorol.* **145** (2), 273–306.

JIMÉNEZ, J. 2012 Cascades in wall-bounded turbulence. *Annu. Rev. Fluid Mech.* **44**, 27–45.

KARNIADAKIS, G.E. & CHOI, K.-S. 2003 Mechanisms on transverse motions in turbulent wall flows. *Annu. Rev. Fluid Mech.* **35** (1), 45–62.

KOLMOGOROV, A.N. 1941 The local structure of turbulence in incompressible viscous fluid for very large Reynolds numbers. *C. R. Acad. Sci. URSS* **30**, 301–305.

LEE, M. & MOSER, R.D. 2015 Direct numerical simulation of turbulent channel flow up to. *J. Fluid Mech.* **774**, 395–415.

https://doi.org/10.1017/jfm.2026.11692 Published online by Cambridge University Press

LI, X., WANG, G. & ZHENG, X. 2021 Logarithmic energy profile of the streamwise velocity for wall-attached eddies along the spanwise direction in turbulent boundary layer. *Phys. Fluids* **33** (10), 105119.
LUNDGREN, T.S. 2002 Kolmogorov two-thirds law by matched asymptotic expansion. *Phys. Fluids* **14** (2), 638–642.
MARUSIC, I. & HEUER, W.D.C. 2007 Reynolds number invariance of the structure inclination angle in wall turbulence. *Phys. Rev. Lett.* **99** (11), 114504.
MARUSIC, I. & HUTCHINS, N. 2008 Study of the log-layer structure in wall turbulence over a very large range of Reynolds number. *Flow Turbul. Combust.* **81**, 115–130.
MARUSIC, I., MCKEON, B.J., MONKEWITZ, P.A., NAGIB, H.M., SMITS, A.J. & SREENIVASAN, K.R. 2010 Wall-bounded turbulent flows at high Reynolds numbers: recent advances and key issues. *Phys. Fluids* **22** (6), 065103.
MARUSIC, I. & MONTY, J.P. 2019 Attached eddy model of wall turbulence. *Annu. Rev. Fluid Mech.* **51**, 49–74.
MARUSIC, I., MONTY, J.P., HULTMARK, M. & SMITS, A.J. 2013 On the logarithmic region in wall turbulence. *J. Fluid Mech.* **716**, R3.
MONIN, A. & OBUKHOV, A.M. 1954 Basic laws of turbulent mixing in the surface layer of the atmosphere. *Contrib. Geophys. Inst. Acad. Sci. USSR* **151** (163), e187.
OBUKHOV, A.M. 1946 Turbulence in an atmosphere with inhomogeneous temperature. *Trudy Inst. Teor. Geofiz. Akad. Nauk SSSR* **1**, 95–115.
PERRY, A.E. & CHONG, M.S. 1982 On the mechanism of wall turbulence. *J. Fluid Mech.* **119**, 173–217.
PERRY, A.E., HENBEST, S. & CHONG, M.S. 1986 A theoretical and experimental study of wall turbulence. *J. Fluid Mech.* **165**, 163–199.
SMITS, A.J., MCKEON, B.J. & MARUSIC, I. 2011 High–Reynolds number wall turbulence. *Annu. Rev. Fluid Mech.* **43**, 353–375.
SREENIVASAN, K.R. & ANTONIA, R.A. 1997 The phenomenology of small-scale turbulence. *Annu. Rev. Fluid Mech.* **29**, 435–472.
TOWNSEND, A.A. 1976 *The Structure of Turbulent Shear Flow*, 2nd edn. Cambridge University Press.
WILCZEK, M., STEVENS, R.J.A.M. & MENEVEAU, C. 2015 Spatio-temporal spectra in the logarithmic layer of wall turbulence: large-eddy simulations and simple models. *J. Fluid Mech.* **769**, R1.
YANG, X.I.A., BAIDYA, R., JOHNSON, P., MARUSIC, I. & MENEVEAU, C. 2017 Structure function tensor scaling in the logarithmic region derived from the attached eddy model of wall-bounded turbulent flows. *Phys. Rev. Fluids* **2** (6), 064602.
YANG, X.I.A., MARUSIC, I. & MENEVEAU, C. 2016 Hierarchical random additive process and logarithmic scaling of generalized high order, two-point correlations in turbulent boundary layer flow. *Phys. Rev. Fluids* **1** (2), 024402.

https://doi.org/10.1017/jfm.2026.11692 Published online by Cambridge University Press